



FeCo–N_x embedded graphene as high performance catalysts for oxygen reduction reaction

Xiaogang Fu^{a,b}, Yanru Liu^{a,b}, Xiaoping Cao^{a,*}, Jutao Jin^b, Qiao Liu^b, Junyan Zhang^{b,**}

^a State Key Laboratory of Applied Organic Chemistry and College of Chemistry and Chemical Engineering, Lanzhou University, Lanzhou 730000, PR China

^b State Key Laboratory of Solid Lubrication, Lanzhou Institute of Chemical Physics, Chinese Academy of Sciences, Lanzhou 730000, PR China

ARTICLE INFO

Article history:

Received 30 July 2012

Received in revised form 8 October 2012

Accepted 29 October 2012

Available online 8 November 2012

Keywords:

Embedded

Graphene

Electrocatalysts

Fuel cells

Oxygen reduction reaction

ABSTRACT

Graphene based non precious metal catalysts for oxygen reduction reaction (ORR) has been successfully fabricated through pyrolysis of a mixture of Fe, Co salts, polyaniline, and reduced graphene oxide (rGO). The transmission electron microscopy (TEM), energy-dispersive X-ray spectroscopy (EDX), Raman spectrum and X-ray photoelectron spectroscopy (XPS) analysis's indicated the transition metal nitrogen-containing moieties (M–N_x, M = Fe or/and Co, x = 2 or 4) could be embedded into the graphene sheets. The electrochemical measurements showed that the embedded M–N_x moieties could act as catalytic sites and boost the activity of catalysts in both acidic and alkaline medium. The effects of Fe and Co on electrochemical properties toward ORR were also investigated, and the results showed the binary metal FeCo–N–rGO was the most active ORR catalyst. Rotating disk electrode measurements revealed that, compared to a commercial Pt/C electrocatalyst (loading: 52.6 μg Pt cm^{−2}), the half-wave potential of the resultant FeCo–N–rGO was 46 mV positive in alkaline medium and 119 mV negative in acidic medium. In addition, the FeCo–N–rGO catalyst was much more stable and tolerant to crossover effect than Pt/C. The above superiorities make it a promising candidate for substituting Pt-based nanomaterials as a cathode catalyst for ORR in fuel cells.

© 2012 Elsevier B.V. All rights reserved.

1. Introduction

The facile availability, natural abundance and environment-friendly of oxygen together with its large electronegativity make oxygen a fascinating cathodic electrode for many batteries, including hydrogen fuel cells, microbial fuel cells and metal-air battery. However, the multiple bonds nature of O₂ molecules makes it chemical inert at low temperature which leads to a sluggish kinetics for the oxygen reduction reaction (ORR) [1]. Catalysts to reduce the energy barrier for ORR are at the heart of these renewable energy devices. Traditionally, platinum-based catalysts have been considered as the most effective catalysts for ORR [2–4]. But their large scale commercial application has been held back by their high cost and scarcity [5]. Apart from these drawbacks, platinum-based catalysts are also subject to their durability and organic molecule deactivation [6]. The development of catalysts with high activity, long-term stability and low cost to supersede platinum-based catalysts for ORR is therefore of paramount importance.

Among the catalysts to reduce or replace platinum-based catalysts for ORR, nitrogen-coordinated transition metals (Fe, Co, Ni and Mn) in a carbon matrix (M–N–C) have been extensively studied owing to their extremely effective catalytic activity for ORR, especially in acidic solution [7–13]. Although the nature of the active sites in such M–N–C catalysts remains elusive, graphene coordinated M–N_x (where x is the coordination number of N atoms to metal) moieties were proposed [14]. However, the performance of fuel cells based on this kind of catalyst is low, one major drawback of the M–N–C catalysts is their poor intrinsic catalytic activity of a single active site (TOF = 0.4 s^{−1}) for ORR compared with Pt (TOF = 25 s^{−1}) [15]. As the overall volumetric activity is the combination of a single site activity and site density, an effective method to increase catalytic activity for M–N–C based catalysts is to increase the active site density. Traditionally, M–N–C based catalysts were prepared by annealing precursors comprising nitrogen, carbon, and naturally abundant transition metals (Fe and Co in particular), however, the active sites only formed on the surface of the carbon support (Fig. 1a) [9]. By ball-milling the precursors before pyrolysis, Lefèvre et al. obtained an electrocatalyst with volumetric activity of 99 A cm^{−3}, matching the performance of state-of-the-art Pt/C catalysts [16]. The ball-milling process is believed to force the precursors into the inner pores of carbon black, and the active sites could be formed on both the surface and inner edge sides of carbon black (Fig. 1b), which greatly increases the active site density [16].

* Corresponding author. Fax: +86 0931 8912582.

** Corresponding author. Fax: +86 0931 4968295.

E-mail addresses: caoxplzu@163.com (X. Cao), zhangjunyan@licp.cas.cn (J. Zhang).

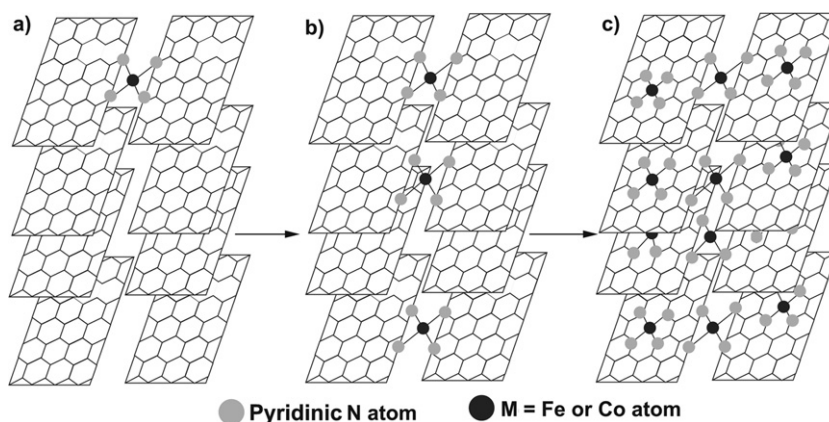


Fig. 1. (a) $M-N_x$ moieties on the surface of carbon black [8]. (b) $M-N_x$ moieties within the carbon black [13]. (c) Proposed schematic structure of $M-N_x$ embedded graphene sheets. The drawing referred the reference [16].

Is it possible to form $M-N-C$ active sites within the carbon support (Fig. 1c), which may further increase the density of the active sites and therefore the catalytic activity for ORR?

Fortunately, both theory calculations and experimental results confirmed that the $M-N_x$ (where x is the coordination number of N atoms to metal) moieties could exist within graphene sheets [17,18]. Duck Hyun Lee and Junbing Yang synthesized carbon nanotubes with $Fe-N_x$ moieties incorporated into their wall sheets and got high catalytic activity [19,20]. However, the harsh experiment conditions of the preparation of CNTs are tedious and not cost-effective for mass production of these catalysts. For the large scale synthesis of $M-N-C$ catalysts with high active site density, graphene, consisting of a two-dimensional (2D) monolayer of graphitic carbon atoms, was used as catalyst support [21]. The disordered nature of graphene oxide makes it favorable for the nitrogen atom dope into graphene sheets by annealing in NH_3 atmosphere [22,23]. When annealing with N-containing polymer, nitrogen with different bonding state, including pyridinic N, pyrrolic N and quaternary N are formed in the graphene sheets [24]. Among the various possible substitutional N, pyridinic N could form defect complexes with carbon vacancies in the graphene [25]. Moreover, only in the presence of divalent metal atoms can the defect complex probably act as anchoring sites for attaching metal (II) to form $M-N_x$ moieties within graphene sheets [17]. Therefore, the $M-N_x$ moieties could be formed both at the edge and within the graphene sheets (Fig. 1c).

To facilitate the incorporation of $M-N_x$ moieties into graphene sheets, nitrogen precursors and transition-metal species had been considered. Polyaniline (PANI) was chosen as nitrogen precursor because the heat treatment could facilitate the incorporation of nitrogen into the graphene sheets to generate more pyridinic N, which could facilitate the formation of $M-N_x$ moieties [24]. In addition, the uniform distribution of nitrogen atoms in PANI may guarantee a more uniform distribution of nitrogen sites in the catalyst and thus increase the density of active sites [26]. Though the Fe or/and Co based nitrogen complexes have long been explored, more exploration of such Fe/Co-N catalysts is necessary to obtain a fundamental understanding of the catalysts structure and active sites.

In this paper, we synthesized graphene-based non precious metal catalysts (NPMCs), into which $M-N_x$ active sites could be probably embedded (Fig. 1c). Generally, a uniform nanocomposite with the polyaniline (PANI) fibers adsorbed on the graphene oxide sheets (GO-PANI) was firstly reduced to rGO-PANI materials [27]. Then, the formentioned materials were mixed with Fe or/and Co salts and pyrolyzed twice to afford the Fe-N-rGO, Co-N-rGO and FeCo-N-rGO

electrocatalysts [28]. The FeCo-N-rGO electrocatalyst indeed exhibits an excellent ORR catalysis, outperforming the carbon-supported Pt catalyst (20 wt% Pt on carbon black, Pt/C) in alkaline medium, and close to the performance of Pt catalyst in acidic medium.

2. Experimental

2.1. Synthesis of $M-N-rGO$

A GO solution was made using modified Hummers method [29,30]. In a typical approach, 5 mL aniline was first dispersed with 500 mL 0.5 M HCl GO solution (1 mg mL^{-1}) [27]. The suspension was kept below 10°C while the oxidant (ammonium peroxydisulfate, APS) and transition metal precursors $FeCl_3$ and $Co(NO_3)_2 \cdot 6H_2O$ were added [26]. After constant mixing for 24 h to allow the polymerized PANI to uniformly mix and cover the GO sheets, the suspension containing GO sheets, polymer and transition metals was heated to 110°C . Then the reducing reagents (1 mL of $NH_3 \cdot H_2O$, 28 w/w in water, and 0.2 mL of N_2H_4 solutions 35 wt% in water) were sequentially inserted at 110°C . After refluxing for 24 h to allow the GO was chemical reduced to rGO, the suspension was vacuum-dried using a rotary evaporator, and then the paste was lyophilized to incompact powder. This powder mixture (FeCo-PANI-rGO) in a ceramic crucible was transferred to the gas tube furnace. The temperature of tube furnace was elevated to 850°C at 5°C min^{-1} of ramping rate and 50 cc min^{-1} of Ar gas flow and held at 850°C for 2 h, which was then cooled to room temperature over ~ 4 h. The heat-treated sample was then pre-leached in 2 M H_2SO_4 at 80°C for 8 h to remove unstable and inactive species from the catalyst, and thoroughly washed in de-ionized water. Finally, the catalyst was heat-treated again in NH_3 atmosphere at 850°C for 30 min before characterization [28,31], which was referred to as “FeCo-N-rGO” catalysts. For comparison, the N-rGO, Fe-N-rGO and Co-N-rGO catalysts were prepared with the same approach but vary the metal precursor.

2.2. Physical characterization

Surface morphologies of FeCo-N-rGO were investigated using SEM (Hitachi S-4800) and TEM (Teana-G2-F30). The XPS data was obtained by using monochromatic Al anode (VG ESCALAB 210). All spectra were calibrated by setting the C 1s photoemission peak for sp^2 -hybridized carbons to 284.5 eV and were fitted after a Shirley type background subtraction.

2.3. Electrochemical measurements

The procedure of glass carbon rotating disk electrode (3 mm in diameter) pretreatment and modification are as follows: the working electrode is polished mechanically with 0.5 μm diamond down to 0.05 μm alumina slurry to obtain a mirror-like surface and then washed with Mill-Q water and EtOH and allowed to dry. Eight milligrams of catalyst powder was dispersed in mixture of 1500 μL of DI water, 420 μL of ethanol, and 80 μL of Nafion (The ink solution, kept in a sealed vial, was sonicated for 5 h). For comparison, a commercially available catalyst of 20 wt% Pt supported on black carbon is used and 4 mg mL^{-1} Pt/C suspension is also prepared as the same procedure described above. Then 5 μL catalyst ink was dropped on a glass carbon rotating disk electrode and was dried at room temperature overnight. This leads to a catalyst loading of 263 $\mu\text{g cm}^{-2}$ and Pt/C of 52.6 $\mu\text{g Pt cm}^{-2}$.

The electrochemical tests were carried out on an AutoLab workstation (μ Autolab III) assembled with a model of ATA-1B rotational system, a conventional three-electrode cell was employed incorporating a working glass carbon RDE, an Ag/AgCl, KCl (saturated) electrode as reference electrode, and a Pt electrode as counter electrode. The backward and forward scans were averaged to remove the capacitive current contribution. The catalysts were tested in 0.1 M KOH and 0.5 M H_2SO_4 solution respectively.

The number of electron (n) transferred was estimated using the Koutecky–Levich equation. The diffusion-limited current density (j_∞) was estimated by the Levich equation (Eq. (1)):

$$j_\infty = 0.62 \cdot F \cdot D_{\text{O}_2}^{\frac{2}{3}} \cdot \nu^{-\frac{1}{6}} \cdot C_{\text{O}_2} \cdot n \cdot \omega^{\frac{1}{2}} = \Gamma \cdot n \cdot \omega^{\frac{1}{2}} \quad (1)$$

$$\Gamma = 0.62 \cdot F \cdot D_{\text{O}_2}^{\frac{2}{3}} \cdot \nu^{-\frac{1}{6}} \cdot C_{\text{O}_2}$$

where F is the Faradaic constant, D is the O_2 diffusion coefficient in the electrolyte, ν is the kinematic viscosity in the electrolyte, C is the O_2 saturation concentration in the electrolyte, n is the number of electrons, and ω is the rotation rate. The physical-chemical parameters of the Levich equation (Γ term in equation 1) were estimated by the measured j_∞ of the ORR on the Pt-RDE, which was assumed to undergo the ideal j_∞ (the direct 4e transfer). In our electrochemical system, j_∞ on the Pt-RDE was measured to $\sim 5.42 \text{ mA cm}^{-2}$ at 1600 rpm and 5 mV s^{-1} in oxygen-saturated 0.1 M KOH (Fig. 7a). Then, the Koutecky–Levich equation was calculated from the following equation (Eq. (2))

$$\frac{1}{j_{\text{measured}}} = \frac{1}{j_\infty} + \frac{1}{j_k} \quad (2)$$

$$\frac{1}{j_{\text{measured}}} = \left(\frac{1}{\Gamma \cdot \frac{1}{n}} \right) \cdot \frac{1}{\omega^{\frac{1}{2}}} + \frac{1}{j_k}$$

where j_k is the kinetic-limited current density and j_{measured} is the current density of catalyst measured using RDE at the same condition of the measured j_∞ . In the Koutecky–Levich plot, $(j_{\text{measured}})^{-1}$ is the y-axis, $\omega^{-1/2}$ is the x-axis, and $(j_k)^{-1}$ indicates the intercept. The n was estimated from the slope. The polarization curves were corrected for diffusion effects by using Eq. (3):

$$j_k = \frac{j_{\text{measured}} \cdot j_\infty}{j_\infty - j_{\text{measured}}} \quad (3)$$

3. Results and discussion

3.1. Physical characterization of the FeCo–N–rGO catalysts

3.1.1. SEM, TEM and EDX investigations

Fig. 2a shows a SEM image of FeCo–N–rGO catalyst, loose network can be observed in the catalyst, and no nanoparticles exist at the tip of the sheets which will be further proved in the following TEM image. After acid washing, the unstable and inactive species can be removed, suggesting that the active sites may be within the rGO sheets not at the surface. As shown in the typical TEM image (Fig. 2b), transparent sheets with wrinkled and folded features are easily observed. Fig. 2c do not reveal the existence of larger crystalline particles like studies of other groups on similar catalysts [32]. On the other hand, the elemental composition analysis from the EDX pattern (Fig. 2d) indicates the presence of elemental N, Fe and Co in FeCo–N–rGO. Therefore, it can be assumed that Fe and Co is present in another form (FeCo– N_x moieties) than in crystalline particles.

3.1.2. Raman investigations

Raman spectra of the rGO, N–rGO, Fe–N–rGO, Co–N–rGO and FeCo–N–rGO composites (Fig. 3) shows two peaks centered at $\sim 1359 \text{ cm}^{-1}$ (D band) and $\sim 1590 \text{ cm}^{-1}$ (G band). The G band is assigned to one of the two E_{2g} modes corresponding to stretching vibrations in the basal plane (sp^2 domains) of single-crystal graphene. The D band is usually attributed to the disorder and imperfection of the carbon crystallites [33]. As can be seen, the increased intensity of the D band for N–rGO, Fe–N–rGO, Co–N–rGO and FeCo–N–rGO indicates that the content of disordered carbon increases after nitrogen doping [34]. Meanwhile, compared FeCo–N–rGO spectra with N–rGO, except for D, G and 2G peaks no other peaks are found, which indicates that no new phase were formed in the catalyst. It is hypothesized that the FeCo– N_x moieties are likely embedded into the graphene sheets.

3.1.3. XPS investigations

XPS spectra of the FeCo–N–rGO sample provide further evidence for the incorporation of N, Fe and Co ions into rGO upon annealing (Fig. 4a). An asymmetric peak centered at 284.5 eV with an extended tail at the higher energy region is fitted to describe the sp^2 -hybridized rGO, as shown in Fig. 4b. The signals of Fe (Fe 2p, 705–735 eV) and Co (Co 2p, 775–805 eV) are shown in Fig. 4c and d. It is postulated that the Fe and Co species may be present in FeCo– N_x form within graphene sheets, any surface Fe and Co oxides, if formed during synthesis, should be dissolved during acid-leaching. The oxidation states of surface iron and cobalt can be interpreted from the spectra, where inactive iron carbides or Fe^0 can be found at 706.7–706.9 and 706.7–707.2 eV, Fe^{2+} at 707.1–708.7 eV, and Fe^{3+} at 710.8–711.8 eV, and for Co 2p the Co^0 and Co^{2+} are at 778.3 eV and 780.4–783.0 eV, respectively [35,36]. The median values of these energies are displayed in Fig. 4c and d as vertical lines. It is clear that Fe^{2+} , Fe^{3+} and Co^{2+} are the dominant species on the catalyst particles, which suggests that the majority of surface iron and cobalt exist in an ionic state. Despite the limited overall understanding of how the metal precursors altered and the nature of the active sites remains elusive [37,38], these surface iron and cobalt ions could potentially be the metal species bound to nitrogen to form FeCo– N_x moieties which could act as active sites [39,40].

The XPS N 1s spectrum of N–rGO, Fe–N–rGO, Co–N–rGO and FeCo–N–rGO reveal the presence of (1) pyridinic N ($\sim 398.3 \text{ eV}$), or (2) nitrile N ($\sim 399.5 \text{ eV}$), (3) pyrrolic N ($\sim 400.4 \text{ eV}$), (4) quaternary N ($\sim 401.3 \text{ eV}$), and (5) oxidized N (~ 402 – 405 eV) [41] (Fig. 5). These samples, which might have acquired N from rGO (some N obtained from the hydrazine heat-treatment) PANI and NH_3 during pyrolysis, show a higher nitrogen amount, and the pyridinic N is

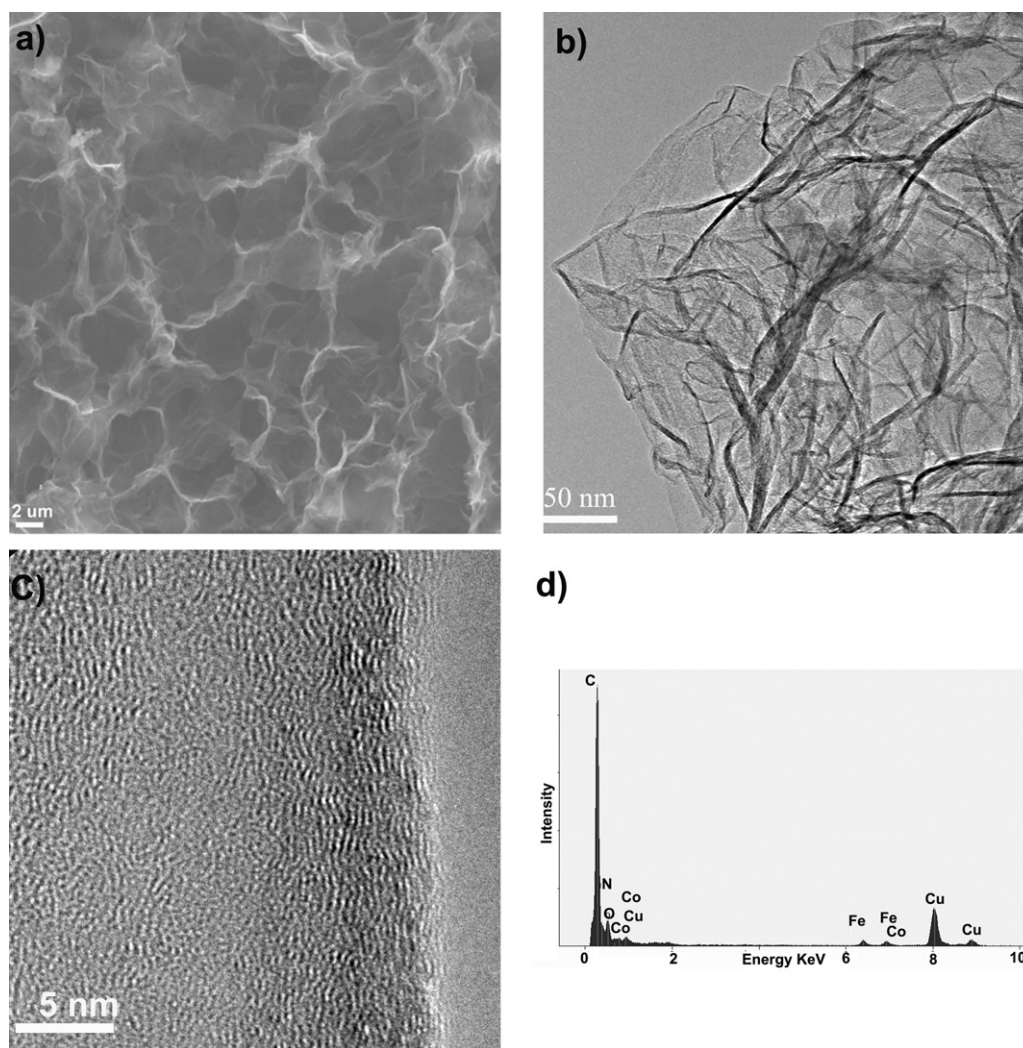


Fig. 2. SEM (a), low-magnification TEM (b), high magnification TEM (c) and EDX of FeCo-N-rGO.

found to be the dominant component for all samples. The high content of pyridinic N could easily form defect complexes with carbon vacancies in the graphene plane, four pyridinic N's and a divacancy could form a porphyrinlike rectangular defect complex. It has also been suggested that the rectangular porphyrinlike rectangular defect in graphene fits very well for a single metal atom with the

oxidation state of (II), resembling the Co-porphyrinlike molecule [17]. On the basis of the high percentage of the pyridinic N species and the presence of Fe 2p and Co 2p peaks in our XPS analysis, one could conclude that these proposed FeCo-N_x moieties could be embedded into the graphene sheets.

The detailed analysis of N1s (Fig. 5) shows remarkable phenomena, the shape of these peaks significantly change when the metal precursors are varied, thus suggesting that different amounts of N configurations were formed at different M-N_x incorporation. The detailed analysis of the relative atomic ratios of each type of N species is shown in Table 1. It is revealed that the total nitrogen content in M-N-rGO is higher than that of N-rGO, which suggests metal ions could facilitate the incorporation of nitrogen. Meanwhile, the pyridinic N is found to be the dominant component for all samples, especially in FeCo-N-rGO catalyst. Analyzed the metal content of these samples, it is surprising that when combined Fe and Co as metal precursors, the content of incorporated Fe and Co in FeCo-N-rGO is higher than that in Fe-N-rGO and Co-N-rGO. It is probably because the Co-N_x moieties are formed more easily in graphene sheets than the Fe-N_x moieties according to previous theory calculations [17]. On the other hand, the Co-N_x moieties may unstable at higher temperature (exceed 700 °C) but the Fe-N_x moieties reach the highest concentration at about 800 °C [42,43]. It is assumed that part of the Co-N_x moieties formed at low temperature could be replaced by Fe-N_x moieties during the pyrolysis

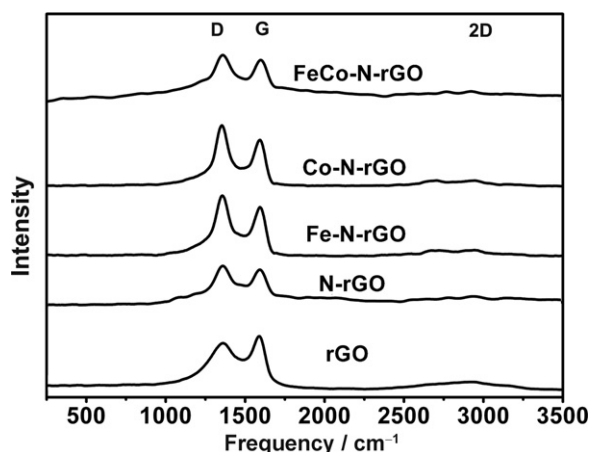


Fig. 3. Raman spectra of rGO, N-rGO, Fe-N-rGO, Co-N-rGO and FeCo-N-rGO.

Table 1

Atomic concentrations (at.%) of Fe, Co, N and heterocyclic N components of N-rGO, Fe-N-rGO, Co-N-rGO and FeCo-N-rGO from XPS analysis.

Sample	Fe	Co	N	Pyridinic N	Nitrile N	Pyrrolic N	Quaternary N
N-rGO	—	—	4.82	1.57	0.74	0.75	1.15
Fe-N-rGO	0.17	—	5.44	1.61	0.9	0.68	1.33
Co-N-rGO	—	0.32	5.73	1.75	0.83	0.65	1.59
FeCo-N-rGO	0.46	0.37	5.86	2.35	1.24	0.78	0.76

process at 850 °C when Fe and Co salt were used as binary metal precursor. It seems like the binary metal precursors could assist embed FeCo-N_x moieties into graphene sheets. Thus, such different amounts of M-N_x configurations in these samples must exert a large influence on their electrocatalytic performances for oxygen reduction.

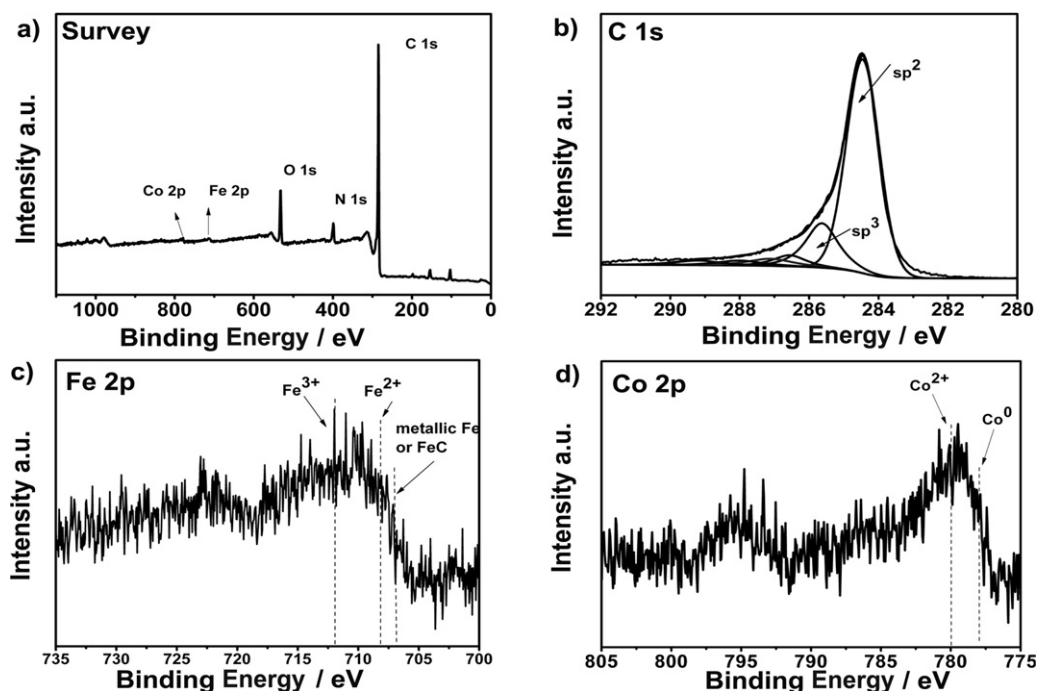
3.2. Electrochemical measurements

The electrocatalytic activity of N-rGO and FeCo-N-rGO materials for ORR was first examined by cyclic voltammetry (CV) in 0.1 M KOH solution saturated with nitrogen or oxygen. As shown in Fig. 6a, featureless voltammetric currents within the potential range from −0.6 to 0.2 V are observed for both electrode materials in the nitrogen-saturated solution. In contrast, both electrode materials show a substantial reduction process in the presence of oxygen, meanwhile the onset and peak potentials of ORR on the FeCo-N-rGO electrode are positive, and the current density is much higher than that of nitrogen only doped rGO electrode. This is probably because not only the isolated N atoms (such as pyridine-like, pyrrole-like, quaternary nitrogen atoms) can act as active sites for ORR but also the FeCo-N_x moieties have higher turnover frequency and hence further enhance the ORR performance.

To gain further insight into the ORR on N-rGO, Fe-N-rGO, Co-N-rGO and FeCo-N-rGO electrodes, rotating disk electrode (RDE) voltammetry (linear-sweep voltammetry, LSV) was performed in oxygen-saturated 0.1 M KOH solution at a scan rate of 5 mV s^{−1} and a rotation rate of 1600 rpm. For comparison, RDE tests were performed on a commercial Pt/C electrode (loading: 52.6 μg Pt cm^{−2}). As shown in Fig. 6b, the single-step wide platform

is observed for the N-rGO, Fe-N-rGO, Co-N-rGO, FeCo-N-rGO and commercial Pt/C electrodes, indicating a direct four-electron ORR process. It can be seen that Fe-N-rGO, Co-N-rGO and FeCo-N-rGO samples have positive onset potential and higher limiting current density than that of the corresponding N-rGO catalyst. The results are in agreement with the CV observations, and further confirm that the M-N_x moieties embedded materials can significantly enhance the ORR catalytic activity. Surprisingly, the FeCo-N-rGO electrode has the lowest onset potential, even lower than that of Pt/C electrode; the half-wave potential of FeCo-N-rGO electrode shifted positively about 46 mV compared to the Pt/C electrode; the diffusion-limiting polarization curves show well-defined plateau and the current density from the FeCo-N-rGO electrode is slight higher than that from the Pt/C electrodes. Together with the Fe-N-rGO, Co-N-rGO characteristics, the superior electrocatalytic ORR activity of FeCo-N-rGO can be attributed to the higher incorporation of pyridinic nitrogen and Fe atoms into the graphene sheets, which suggests that the embedded M-N_x moieties play an important role in the ORR activity especially the Fe-N_x moieties. Therefore, the above RDE experiments confirm that the novel FeCo-N-rGO is the best ORR catalyst, even better than the commercial Pt/C, in performance.

The LSV curves of Pt/C and FeCo-N-rGO catalysts at different rotation speeds, the Koutecky–Levich plots and the Tafel plots are presented in Fig. 6. The Koutecky–Levich plots at various potentials exhibit good linearity and parallelism for FeCo-N-rGO and Pt/C catalysts, indicating first-order reaction kinetics for ORR with respect to the concentration of dissolved oxygen. The electron transfer number (*n*) was calculated to be ~3.9 at −0.20 to −0.40 V (Fig. 6f) from the slopes of Koutecky–Levich plots

**Fig. 4.** XPS spectra of FeCo-N-rGO powders in the survey, C 1s, Fe 2p, Co 2p.

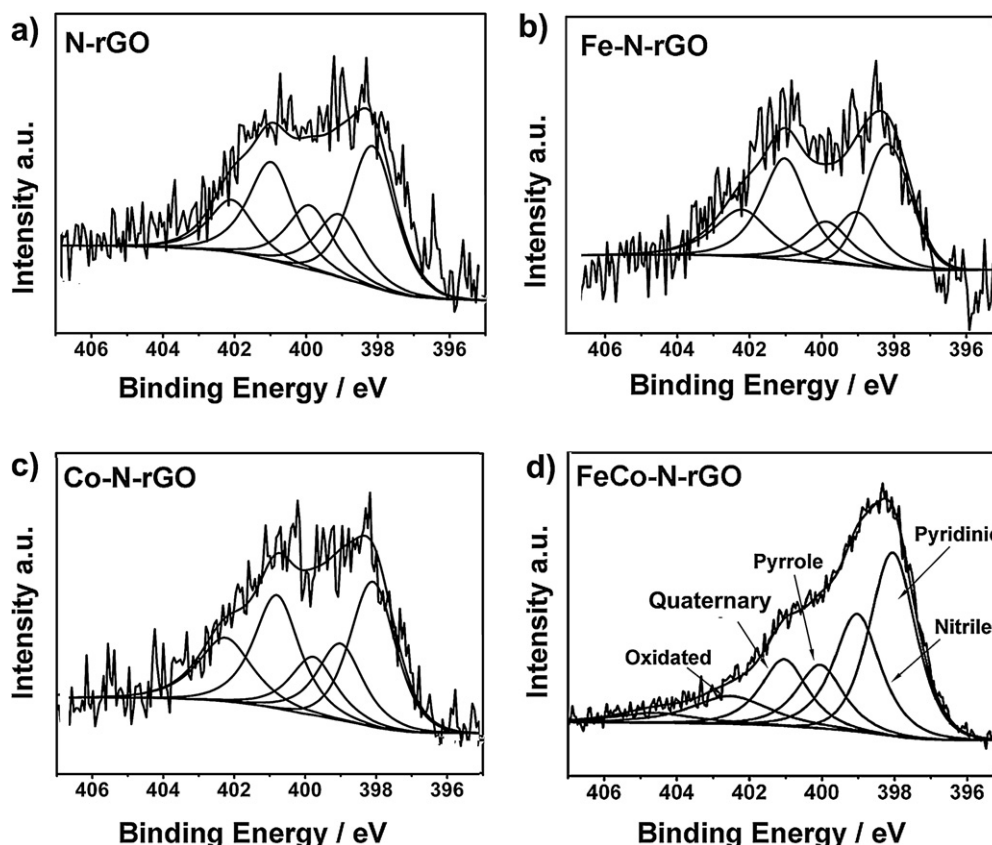


Fig. 5. N 1s XPS spectra of N-rGO, Fe-N-rGO, Co-N-rGO and FeCo-N-rGO.

(Eqs. (1) and (2)), suggesting FeCo-N-rGO favors a 4e oxygen reduction process, similar to ORR catalyzed by a high-quality commercial Pt/C catalyst measured in the same 0.1 M KOH electrolyte ($n=4.0$ for Pt/C, Fig. 6d). By using Eq. (3) the polarization curves were corrected for diffusion effects. As reported by previous studies [44,45], two distinct Tafel slopes in low and high overpotentials regions were obtained on Tafel plots of Pt/C and FeCo-N-rGO. The estimated Tafel slopes in low and high regions of Pt/C catalyst are -62 and -127 mV decade $^{-1}$ (Fig. 6g), respectively, which are close to the usually reported values for ORR on Pt electrode [46]. The Tafel slopes of FeCo-N-rGO were calculated to be -70 and -134 mV decade $^{-1}$ in low and high overpotentials regions (Fig. 6h) and are very close to the values of Pt/C catalyst. One reasonable interpretation for this result is that the embedded FeCo-N_x moieties are more catalytically active during the ORR process. Thus, the FeCo-N-rGO electrode shows high diffusion-limiting current density, high electron transfer number (~ 3.9) and high positive half-wave potential, which already outperforms the commercial Pt/C electrocatalyst for ORR in alkaline electrolyte.

In view of the potential of FeCo-N-rGO as effective ORR catalysts to replace the commercially available Pt/C electrode, we further tested the electrochemical stability, possible methanol crossover. The current–time (i – t) chronoamperometric response for ORR at the Pt/C electrode shows a sharp decrease in current on addition of 3.0 M methanol for the Pt/C electrode (Fig. 7a). In contrast, the amperometric response from the FeCo-N-rGO electrode remains almost unchanged even after the addition of methanol. Therefore, the FeCo-N-rGO electrode has a higher selectivity toward ORR and better methanol tolerance than the commercial Pt/C electrocatalyst. Then, the durability of the FeCo-N-rGO and commercial Pt/C electrodes for ORR was evaluated via a chronoamperometric method at -0.3 V in an oxygen-saturated 0.1 M KOH at a rotation

rate of 1600 rpm, and all the data were recorded after the electrodes had worked 30 min in order to dissolve non-reactive phase of the catalyst. As seen in Fig. 7b, the current density both the FeCo-N-rGO and Pt/C electrodes cause only a slight loss ($\sim 7\%$), indicating that the FeCo-N-rGO electrocatalyst is more stable than the commercial Pt/C electrode. The stability could be attributed to the covalent incorporation of FeCo-N_x moieties into graphene sheets, especially the Co-N_x moiety that performs more stability than Fe-N_x moiety on working conditions [47].

Finally, the activity of N-rGO and FeCo-N-rGO in 0.5 M H₂SO₄ was also tested in this paper. In 0.5 M H₂SO₄, featureless voltammetric curves are similarly observed in the nitrogen saturated solution, but only FeCo-N-rGO electrode shows pronounced cathodic peak in oxygen-saturated solution. (Fig. 8a) The subsequent RDE experiments show that the N-rGO and the Fe-N-rGO electrodes exhibit lower ORR activity and Co-N-rGO and FeCo-N-rGO electrodes show higher activity (Fig. 8b). It is probably because that the ORR activity in acidic medium is mainly depends on the M-N_x moieties [48,49], because protonation reaction of isolated pyridinic N in acidic medium could lead to the ORR activity loss and only the M-N_x moieties are stable [50]. Therefore, with no M-N_x moieties in the N-rGO and a lower concentration of Fe-N_x moieties in the Fe-N-rGO, these two catalysts show inferior ORR performance. The enhanced activity of Co-N-rGO and FeCo-N-rGO could be attributed to the incorporation of M-N_x especially the Fe-N_x moieties. The performance gap between a state-of-the-art Pt/C and FeCo-N-rGO, expressed as a half-wave potential difference in rotating disk electrode test, remain has 119 mV relative to Pt/C at a loading of $52.6 \mu\text{g Pt cm}^{-2}$ (Fig. 8b). Though the catalyst shows lower activity in acidic medium than that in alkaline medium, it remains a one step, 4e transfer pathway (Fig. 8f). For FeCo-N-rGO, the Tafel slope values of -81 mV decade $^{-1}$ and

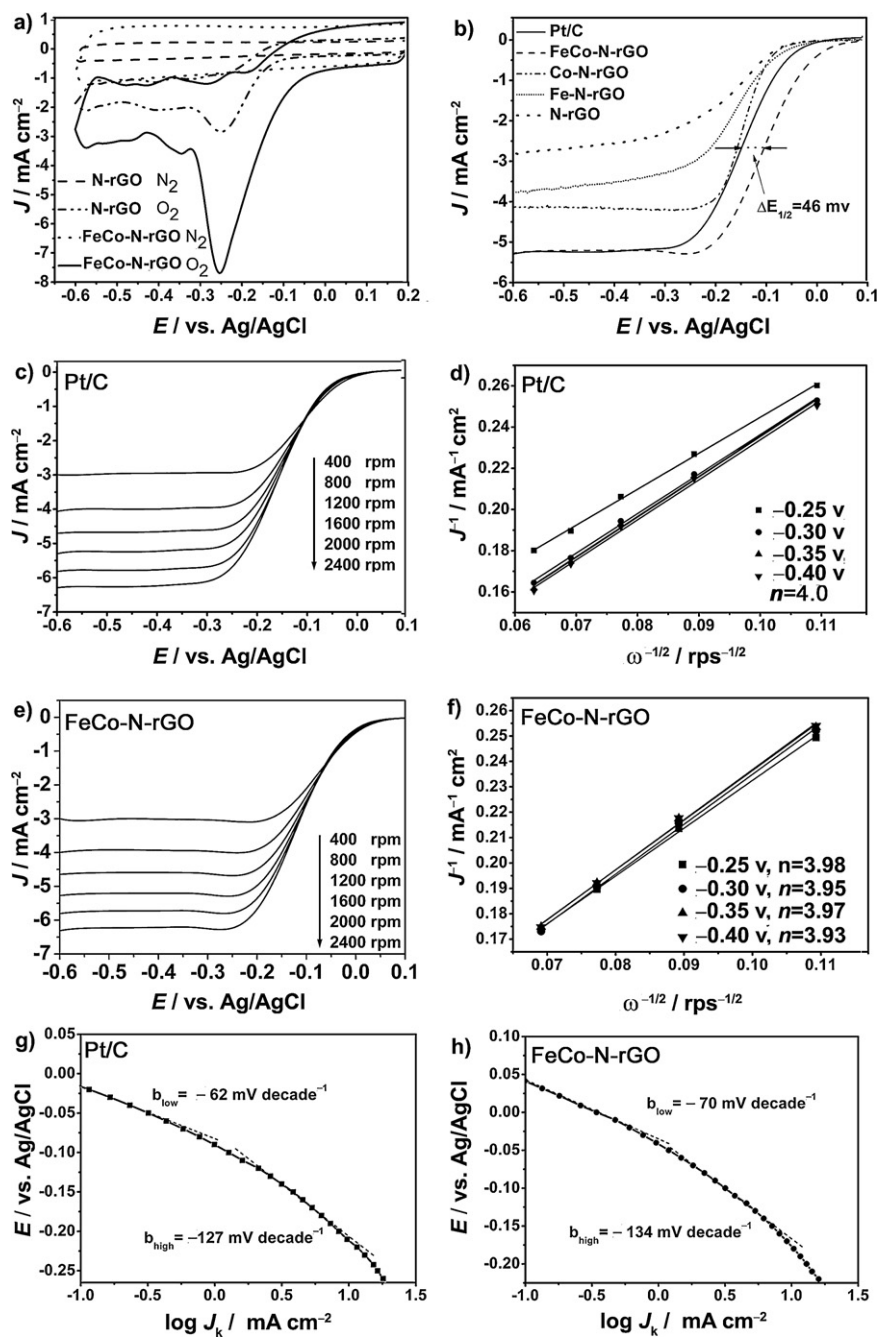


Fig. 6. (a) Cyclic voltammograms of N-rGO and FeCo-N-rGO electrodes were tested in nitrogen and oxygen saturated 0.1 M KOH aqueous electrolyte solutions at a scan rate of 50 mV s⁻¹. (b) LSV curves of N-rGO, Fe-N-rGO, Co-N-rGO, FeCo-N-rGO and Pt/C electrodes. LSV curves with various rotation rates, Koutecky-Levich plots and Tafel plots of (c, d, g) Pt/C electrode, (e, f, h) FeCo-N-rGO electrode. All the LSV curves were tested in oxygen saturated 0.1 M KOH electrolyte at a scan rate of 5 mV s⁻¹.

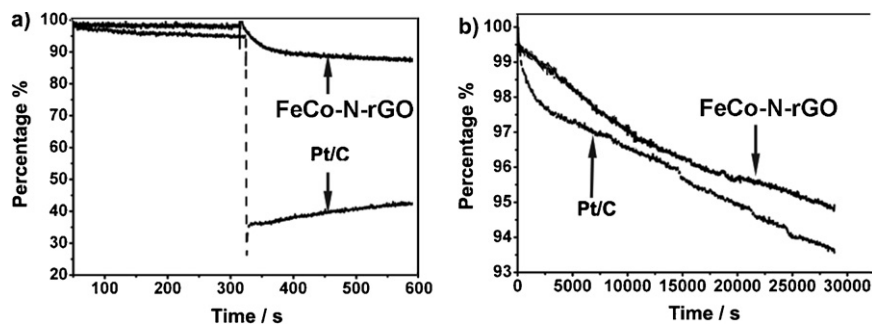


Fig. 7. Chronoamperometric response for ORR at FeCo-N-rGO and Pt/C electrodes (a) on addition of 3 M methanol after about 300 s and (b) durability evaluation of Pt/C and FeCo-N-rGO electrodes for 30,000 s at -0.30 V vs. and a rotation rate of 1600 rpm.

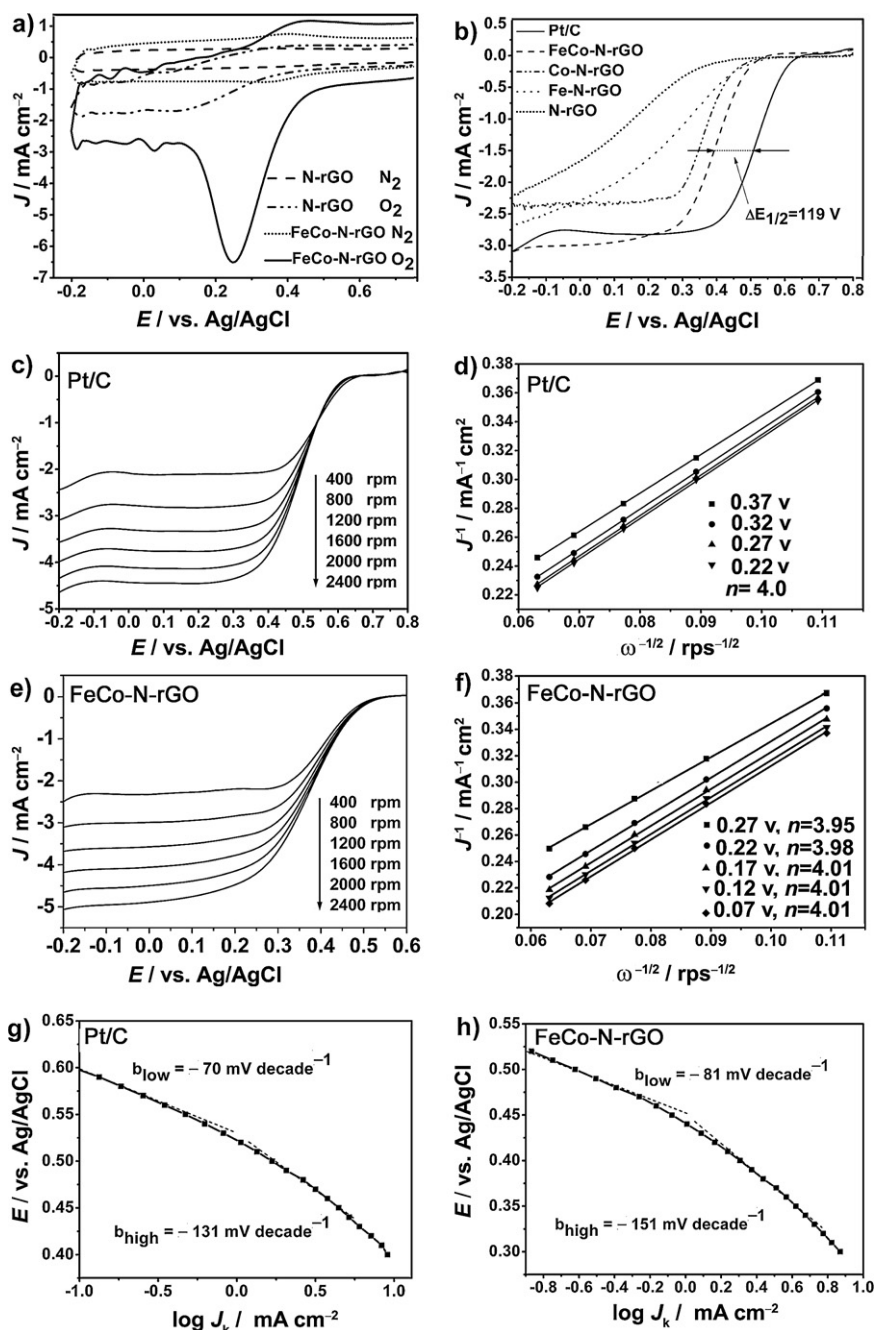


Fig. 8. (a) Cyclic voltammograms of N-rGO and FeCo-N-rGO electrodes were tested in nitrogen and oxygen saturated 0.5 M H₂SO₄ aqueous electrolyte solutions at a scan rate of 50 mV s⁻¹. (b) LSV curves of N-rGO, Fe-N-rGO, Co-N-rGO, FeCo-N-rGO and Pt/C electrodes. LSV curves with various rotation rates, Koutecky–Levich plots and Tafel plots of (c, d, g) Pt/C electrode, (e, f, h) FeCo-N-rGO electrode. The LSV curves were tested in oxygen saturated 0.5 M H₂SO₄ electrolyte at a scan rate of 10 mV s⁻¹ and a rotation rate of 800 rpm.

–151 mV decade⁻¹ in low and high overpotentials regions (Fig. 8h) were higher than that of Pt/C catalysts (–70 mV decade⁻¹ and –131 mV decade⁻¹, Fig. 8g). A higher Tafel slope (absolute value) reveals that overpotential increases quickly with current density, leading to slightly inferior ORR activity [46]. Since the electrocatalytic activity of the M–N–rGO toward ORR is considerably affected by the alteration of M–N_x content in graphene sheets, it would be advantageous to identify a suitable strategy to afford abundant defects on the graphene sheets to increase the number of catalytic sites therefore enhance the ORR activity. The work on improving the synthetic approach to make the ORR activity close to Pt/C in acidic medium is under taking.

4. Conclusion

In summary, we have demonstrated an effective approach for the large scale fabrication of graphene based NPMCs for the oxygen reduction reaction through pyrolysis activation. SEM, TEM, EDX, Raman, and XPS were adopted to characterize the graphene-based catalysts, and the results indicated the M–N_x moieties could be embedded into the graphene sheets. Based on the experimental results, it is concluded that the Co–N_x moieties could facilitate the incorporation of Fe–N_x moieties during the pyrolysis process and the content of Fe–N_x active sites in rGO sheets plays a key role for ORR activity. In comparison to the commercial Pt/C

catalyst, FeCo–N–rGO catalyst presented higher ORR onset potential and 46 mV more positive ORR half-wave potential in alkaline solution. Importantly, it also demonstrated good tolerance to methanol and better stability than Pt/C (loading: $52.6 \mu\text{g Pt cm}^{-2}$) in the studied conditions. Though the FeCo–N_x embedded graphene material showed lower ORR performance compared to Pt/C in acidic solution at present, it certainly deserve to further study and may have the potential to replace the Pt/C catalyst in fuel cells.

Acknowledgement

This work was supported by National Nature Science Foundation of China (grant no. 50823008).

References

- [1] K. Lee, L. Zhang, J. Zhang, in: J. Zhang (Ed.), *PEM Fuel Cell Electrocatalysts and Catalyst Layers*, Springer, London, 2008, pp. 715–757.
- [2] B. Lim, M. Jiang, P.H.C. Camargo, E.C. Cho, J. Tao, X. Lu, Y. Zhu, Y. Xia, *Science* 324 (2009) 1302.
- [3] V.R. Stamenkovic, B. Fowler, B.S. Mun, G. Wang, P.N. Ross, C.A. Lucas, N.M. Marković, *Science* 315 (2007) 493–497.
- [4] N.R. Elezovic, B.M. Babic, P. Ercius, V.R. Radmilovic, L.M. Vracar, N.V. Krstajic, *Applied Catalysis B: Environmental* 125 (2012) 390–397.
- [5] D. Sebastián, A.G. Ruíz, I. Suelves, R. Moliner, M.J. Lázaro, V. Baglio, A. Stassi, A.S. Arico, *Applied Catalysis B: Environmental* 115–116 (2012) 269–275.
- [6] M. Winter, R.J. Brodd, *Chemical Reviews* 104 (2004) 4245–4270.
- [7] M. Yuasa, A. Yamaguchi, H. Itsuki, K. Tanaka, M. Yamamoto, K. Oyaizu, *Chemistry of Materials* 17 (2005) 4278–4281.
- [8] X. Yuan, X. Zeng, H.-J. Zhang, Z.-F. Ma, C.-Y. Wang, *Journal of the American Chemical Society* 132 (2010) 1754–1755.
- [9] A. Velázquez-Palenzuela, L. Zhang, L. Wang, P.L. Cabot, E. Brillas, K. Tsay, J. Zhang, *Electrochimica Acta* 56 (2011) 4744–4752.
- [10] C.W.B. Bezerra, L. Zhang, K. Lee, H. Liu, A.L.B. Marques, E.P. Marques, H. Wang, J. Zhang, *Electrochimica Acta* 53 (2008) 4937–4951.
- [11] C.H. Choi, S.H. Park, S.I. Woo, *Applied Catalysis B: Environmental* 119–120 (2012) 123–131.
- [12] A. Morozan, P. Jegou, B. Jousset, S. Palacin, *Physical Chemistry Chemical Physics* 13 (2011) 21600–21607.
- [13] D. Nguyen-Thanh, A.I. Frenkel, J. Wang, S. O'Brien, D.L. Akins, *Applied Catalysis B: Environmental* 105 (2011) 50–60.
- [14] M. Lefèvre, J.P. Dodelet, P. Bertrand, *Journal of Physical Chemistry B* 109 (2005) 16718–16724.
- [15] H.A. Gasteiger, N.M. Marković, *Science* 324 (2009) 48–49.
- [16] M. Lefèvre, E. Proietti, F. Jaouen, J.-P. Dodelet, *Science* 324 (2009) 71–74.
- [17] W.I. Choi, S.-H. Jhi, K. Kim, Y.-H. Kim, *Physical Review B* 81 (2010) 085441.
- [18] F. Calle-Vallejo, J.I. Martínez, J. Rossmeisl, *Physical Chemistry Chemical Physics* 13 (2011) 15639.
- [19] J. Yang, D.-J. Liu, N.N. Kariuki, L.X. Chen, *Chemical Communications* (2008).
- [20] D.H. Lee, W.J. Lee, W.J. Lee, S.O. Kim, Y.-H. Kim, *Physical Review Letters* 106 (2011) 175502.
- [21] E. Antolini, *Applied Catalysis B: Environmental* 123–124 (2012) 52–68.
- [22] X. Li, H. Wang, J.T. Robinson, H. Sanchez, G. Diankov, H. Dai, *Journal of the American Chemical Society* 131 (2009) 15939–15944.
- [23] Z.-H. Sheng, L. Shao, J.-J. Chen, W.-J. Bao, F.-B. Wang, X.-H. Xia, *ACS Nano* 5 (2011) 4350–4358.
- [24] I. Lai, J. Potts, D. Zhan, L. Wang, C.K. Poh, C. Tang, H. Gong, Z. Shen, J. Lin, R. Ruoff, *Energy and Environmental Science* 5 (2012) 7936–7942.
- [25] S.B. Zhang, J.E. Northrup, *Physical Review Letters* 67 (1991) 2339–2342.
- [26] G. Wu, K.L. More, C.M. Johnston, P. Zelenay, *Science* 332 (2011) 443–447.
- [27] C. Valleis, P. Jimeñez, E. Muñoz, A.M. Benito, W.K. Maser, *Journal of Physical Chemistry C* 115 (2011) 10468–10474.
- [28] U.I. Kramm, I. Herrmann-Geppert, P. Bogdanoff, S. Fiechter, *Journal of Physical Chemistry C* 115 (2011) 23417–23427.
- [29] W.S. Hummers, R.E. Offeman, *Journal of the American Chemical Society* 80 (1958) 1339.
- [30] H.-L. Guo, X.-F. Wang, Q.-Y. Qian, F.-B. Wang, X.-H. Xia, *ACS Nano* 3 (2009) 2653–2659.
- [31] F. Jaouen, E. Proietti, M. Lefèvre, R. Chenitz, J.-P. Dodelet, G. Wu, H.T. Chung, C.M. Johnston, P. Zelenay, *Energy and Environmental Science* 4 (2011) 114.
- [32] H.R. Byon, J. Suntivich, Y. Shao-Horn, *Chemistry of Materials* 23 (2011) 3421–3428.
- [33] K.N. Kudin, B. Ozbas, H.C. Schniepp, R.K. Prud'homme, I.A. Aksay, R. Car, *Nano Letters* 8 (2007) 36–41.
- [34] Y. Shao, S. Zhang, M.H. Engelhard, G. Li, G. Shao, Y. Wang, J. Liu, I.A. Aksay, Y. Lin, *Journal of Materials Chemistry* 20 (2010) 7491.
- [35] G. Faubert, R. Côté, J.P. Dodelet, M. Lefèvre, P. Bertrand, *Electrochimica Acta* 44 (1999) 2589–2603.
- [36] S. Li, L. Zhang, J. Kim, M. Pan, Z. Shi, J. Zhang, *Electrochimica Acta* 55 (2010) 7346–7353.
- [37] Z. Chen, D. Higgins, A. Yu, L. Zhang, J. Zhang, *Energy and Environmental Science* 4 (2011) 3167.
- [38] M. Lefèvre, J.P. Dodelet, P. Bertrand, *Journal of Physical Chemistry B* 104 (2000) 11238–11247.
- [39] J. Wu, W. Li, D. Higgins, Z. Chen, *Journal of Physical Chemistry C* 115 (2011) 18856–18862.
- [40] M. Ferrandon, A.J. Kropf, D.J. Myers, K. Artyushkova, U. Kramm, P. Bogdanoff, G. Wu, C.M. Johnston, P. Zelenay, *Journal of Physical Chemistry C* 116 (2012) 16001–16013.
- [41] F. d. r. Jaouen, J. Herranz, M. Lefèvre, J.-P. Dodelet, U.I. Kramm, I. Herrmann, P. Bogdanoff, J. Maruyama, T. Nagaoka, A. Garsuch, J.R. Dahn, T. Olson, S. Pylypenko, P. Atanassov, E.A. Ustinov, *ACS Applied Materials and Interfaces* 1 (2009) 1623–1639.
- [42] J.M. Ziegelbauer, T.S. Olson, S. Pylypenko, F. Alamgir, C. Jaye, P. Atanassov, S. Mukerjee, *Journal of Physical Chemistry C* 112 (2008) 8839–8849.
- [43] M. Lefèvre, J.P. Dodelet, P. Bertrand, *Journal of Physical Chemistry B* 106 (2002) 8705–8713.
- [44] J. Liang, Y. Zheng, J. Chen, J. Liu, D. Hulicova-Jurcakova, M. Jaroniec, S.Z. Qiao, *Angewandte Chemie International Edition* 51 (2012) 3892–3896.
- [45] R. Kothandaraman, V. Nallathambi, K. Artyushkova, S.C. Barton, *Applied Catalysis B: Environmental* 92 (2009) 209–216.
- [46] G. Ma, R. Jia, J. Zhao, Z. Wang, C. Song, S. Jia, Z. Zhu, *Journal of Physical Chemistry C* 115 (2011) 25148–25154.
- [47] R. Liu, C. von Malotki, L. Arnold, N. Koshino, H. Higashimura, M. Baumgarten, K. Müllen, *Journal of the American Chemical Society* 133 (2011) 10372–10375.
- [48] Y. Li, W. Zhou, H. Wang, L. Xie, Y. Liang, F. Wei, J.-C. Idrobo, S.J. Pennycook, H. Dai, *Nature Nanotechnology* 7 (2012) 394–400.
- [49] J.-P. Dodelet, U. Kramm, J. Herranz, N. Larouche, T. Arruda, m. lefevre, F. Jaouen, P. Bogdanoff, S. Fiechter, I. Abs-Wurmbach, S. Mukerjee, *Physical Chemistry Chemical Physics* 14 (2012) 11673–11688.
- [50] J. Herranz, F. d. r. Jaouen, M. Lefèvre, U.I. Kramm, E. Proietti, J.-P. Dodelet, P. Bogdanoff, S. Fiechter, I. Abs-Wurmbach, P. Bertrand, T.M. Arruda, S. Mukerjee, *Journal of Physical Chemistry C* 115 (2011) 16087–16097.